

Observation of a zero-energy excitation mode in the open Dicke model

Anton Bölian,^{1,*} Phatthamon Kongkhambut,^{1,2,3,*} Christoph Georges,¹ Roy D. Jara Jr.,⁴ José Vargas,¹ Jens Klinder,¹ Jayson G. Cosme,⁴ Hans Keßler,^{1,†} and Andreas Hemmerich^{1,5,‡}

¹*Center for Optical Quantum Technologies and Institute for Quantum Physics, Universität Hamburg, 22761 Hamburg, Germany*

²*Quantum Simulation Research Laboratory, Department of Physics and Materials Science,*

Faculty of Science, Chiang Mai University, Chiang Mai, 50200, Thailand

³*Thailand Center of Excellence in Physics, Office of the Permanent Secretary, Ministry of Higher Education, Science, Research and Innovation, Thailand*

⁴*National Institute of Physics, University of the Philippines, Diliman, Quezon City 1101, Philippines*

⁵*The Hamburg Center for Ultrafast Imaging, Luruper Chaussee 149, 22761 Hamburg, Germany*

(Dated: February 18, 2025)

Approaching phase boundaries in many-body systems can give rise to intriguing signatures in their excitation spectra. Here, we explore the excitation spectrum of a Bose-Einstein condensate strongly coupled to an optical cavity and pumped by an optical standing wave, which simulates the famous Dicke-Hepp-Lieb phase transition of the open Dicke model with dissipation arising due to photon leakage from the cavity. For weak dissipation, the excitation spectrum displays two strongly polaritonic modes. Close to the phase boundary, we observe an intriguing regime where the lower-energetic of these modes, instead of showing the expected roton-type mode softening, is found to approach and persist at zero energy, well before the critical pump strength for the Dicke-Hepp-Lieb transition boundary is reached. Hence, a peculiar situation arises, where an excitation is possible at zero energy cost, but nevertheless no instability of the system is created.

The coupling of a quantum gas to an optical cavity provides an ideal experimental scenario to study the effects of strong light-matter interactions [1, 2], including cavity-induced cooling [3–5], cavity optomechanics [6–10], and quantum simulations of many-body physics [11–16]. Atom-cavity systems can also be used to emulate the open Dicke model [17], in which an ensemble of identical two-level systems is coupled to a single mode of the electromagnetic field. In cavity QED, the open Dicke model is typically realised by coupling the atomic ensemble to a single cavity mode, while the system interacts with the environment via photons leaking out of the cavity with the cavity field decay rate κ . This has been achieved with thermal atoms [18] and both fermionic [19–22] and bosonic [23–25] quantum gases. In the recoil-resolved regime, when the cavity bandwidth is smaller than the recoil frequency ω_{rec} , atom-cavity systems provide access to several distinctive phenomena, such as discrete [13, 26–28] and continuous [14, 29–31] time crystals.

The open Dicke model hosts a continuous phase transition, where the atoms reorganize from interacting individually with the cavity mode to forming a macroscopic dipole moment that collectively interacts with the cavity mode [32]. It can be experimentally implemented using a Bose-Einstein condensate (BEC) strongly coupled to a longitudinal mode of an optical Fabry-Pérot type cavity, which is pumped by a retro-reflected laser beam with frequency ω_p and strength ϵ_p , aligned perpendicularly to the cavity mode. In this configuration, the phase transition is characterized by the atoms spontaneously self-organizing in one of two possible density-wave configurations above a critical pump strength. These density gratings enable efficient Bragg scattering of light from the transverse pump field into the cavity and vice versa [23, 33, 34]. In a many-body picture, this transition can be understood as the result of tuning the strength of a light-induced infinite-range inter-

action (LIRI) between the atoms. In the specific case studied here, the atom-cavity system has an extremely narrow bandwidth, i.e., the photon loss rate of the cavity is on the order of the recoil frequency ω_{rec} such that the time scales for the evolution in the light and matter sectors are comparable and hence the LIRI among the atoms is significantly retarded. To investigate this phase transition in the retarded LIRI regime, we study the excitation energy of the polariton modes for pump strengths ϵ_p below the critical threshold. The case of instantaneous LIRI, arising for a broad-bandwidth atom-cavity system, has been previously explored in [35]. In the instantaneous LIRI regime, only the far detuned case $|\delta_{\text{eff}}| \gg \omega_{\text{rec}}$ is possible because $|\delta_{\text{eff}}| > \kappa$ and $\kappa \gg \omega_{\text{rec}}$. This leads to a single observable weakly polaritonic excitation mode, which features a strongly dominating matter component. The recoil-resolution of our cavity ($\kappa \sim \omega_{\text{rec}}$) [10, 33] provides us access to a regime where the effective pump-cavity detuning is comparable to the recoil frequency $\delta_{\text{eff}} \sim -2\omega_{\text{rec}}$. In this near-resonant regime, we expect the formation of two strongly polaritonic modes, which are composed of comparable admixtures of photonic and matter components.

In this work, we investigate two cases within the near-resonant regime. For $|\delta_{\text{eff}}| \gtrsim 2\omega_{\text{rec}}$, the lower energetic polariton mode shows the expected roton-type mode softening character, i.e., its excitation frequency approaches zero when the pump threshold for self-organisation is reached. This behavior is also found in the instantaneous LIRI regime [35]. If, however, $|\delta_{\text{eff}}| \lesssim 2\omega_{\text{rec}}$, the lower energetic polariton acquires an overdamped character such that its excitation resonance frequency ω_{exc} falls to zero clearly before self-organisation occurs. This intriguing finding points out that a situation can arise, where an excitation costs zero energy but nevertheless does not create an instability of the system. For both regimes we will also discuss the distinct behaviors with

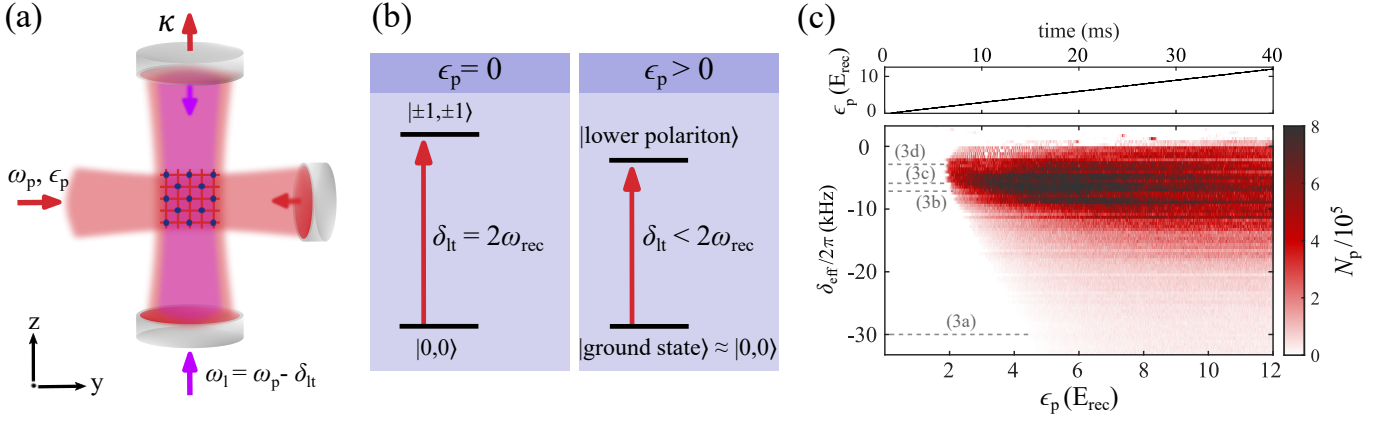


FIG. 1. (a) Illustration of the Bragg spectroscopy scheme applied to our atom-cavity system to probe the excitation energy of the polariton modes using the transverse pump with frequency ω_p and pump strength ϵ_p and the on-axis longitudinal pump with a varying detuning δ_{it} with respect to the transverse pump. (b) Sketch of the mode softening of the lower polariton mode as the transverse pump strength increases. (c) Intracavity photon number N_p plotted against the effective detuning δ_{eff} between the transverse pump and the cavity and the transverse pump strength ϵ_p , with the detunings at which the excitation spectra shown in Fig.3 were measured ($\delta_{\text{eff}} = 2\pi \times \{-30, -7.5, -6, -3\}$ kHz) marked accordingly. For negative effective detunings $\delta_{\text{eff}} < 0$, the formation of a finite intracavity light field N_p arising above a critical value of the transverse pump strength ϵ_p indicates that the system self-organises into a superradiant phase.

regard to the higher energetic polariton modes.

In our experiment, a BEC of $N_a \approx 40 \times 10^3$ ^{87}Rb atoms is strongly coupled to a single mode of an optical cavity with a finesse of 4.2×10^5 . The atoms are primarily addressed with a retro-reflected laser beam with frequency ω_p , transversely oriented with respect to the cavity axis, referred to in the following as the transverse pump. This setup is depicted in Figure 1(a). The pump wavelength $\lambda_p = 803.26$ nm is far-red detuned with respect to the relevant atomic transitions, namely the D_1 and D_2 lines at 794.97 and 780.24 nm, respectively, thus we operate in the dispersive regime. At this chosen pump wavelength, the transverse pump produces an attractive standing-wave potential at the position of the atoms. In this experiment, we utilise a cavity that operates in the recoil-resolved regime, where the field decay rate of $\kappa = 2\pi \times 3.60$ kHz is comparable to the recoil frequency $\omega_{\text{rec}} = 2\pi \times 3.55$ kHz [10]. The cavity resonance is shifted as a result of the refractive index of the BEC in the cavity by an amount $\delta_- = N_a U_0 / 2$, where $U_0 = -2\pi \times 0.34$ Hz is the dispersive shift per atom. We therefore define an effective detuning with respect to the cavity resonance of $\delta_{\text{eff}} = \delta_c - \delta_-$, where $\delta_c = \omega_p - \omega_c$ is the detuning of the transverse pump frequency ω_p with respect to the empty cavity resonance frequency ω_c . In this experimental platform, the two-level systems at the basis of the open Dicke model are atomic momentum modes, with the zero momentum mode $|p_y, p_z\rangle \equiv |0, 0\rangle$, referred to as the BEC mode, forming the ground state, and a superposition $|\pm 1, \pm 1\rangle \equiv \sum_{\nu, \mu \in \{-1, +1\}} |\nu \hbar k, \mu \hbar k\rangle$ of $|\pm \hbar k, \pm \hbar k\rangle$ momentum modes forming the excited state. Here, the same wavenumber $k = 2\pi/\lambda_p$ is assumed for both the transverse and the longitudinal pump waves, which is justified due to their comparatively small detunings on the scale of a few kHz. When the transverse pump is red-detuned with respect to the cavity resonance ($\delta_{\text{eff}} < 0$) and its pump strength ϵ_p exceeds a

critical value ϵ_c , the atomic ensemble self-organises from the normal phase (NP), a BEC in a standing wave pump potential, into one of two density lattice configurations in the superradiant (SR) phase [13, 34], resulting in the build-up of a finite intracavity light field with photon number N_p . By measuring the number of photons N_p leaking out of the cavity with a heterodyne detector for a fixed δ_{eff} as the transverse pump strength ϵ_p is increased, we obtain the phase diagram shown in Figure 1(c). It should be noted that the critical pump strength ϵ_c varies with δ_{eff} .

To theoretically analyse the system as it approaches the phase transition, we study the excitation energy of the polaritonic modes by performing a stability analysis. In this model, we only take into account the occupation of the two lowest momentum modes, $|0, 0\rangle$ and $|\pm 1, \pm 1\rangle$, which we refer to as the two-mode stability analysis [25]. We perform this analysis for a fixed δ_{eff} to determine the excitation energy $E_{\text{exc}} = \hbar \omega_{\text{exc}}$ and excitation rate γ of the polariton modes, resulting from the real and imaginary parts of the eigenvalues of the stability matrix, respectively. Further details on the stability analysis and the stability matrix itself are provided in the supplemental material [36]. For zero transverse pump strength $\epsilon_p = 0$ the atomic and photonic modes are decoupled, the energy required to excite the atoms from the $|0, 0\rangle$ into the $|\pm 1, \pm 1\rangle$ momentum modes is $2\hbar \omega_{\text{rec}}$, and the energy required to excite the cavity mode is $|\hbar \delta_{\text{eff}}|$, see Figure 1(b). As the transverse pump strength increases, the off-diagonal terms in the stability matrix become nonzero, and the stability matrix obtains two new eigenstates, composed of mixed atom-light excitations, referred to as the upper and lower polariton modes. The excitation energy of the lower polariton mode reaching zero is a necessary but not sufficient requirement for spontaneously transitioning into the SR phase. The second necessary criterion is a positive

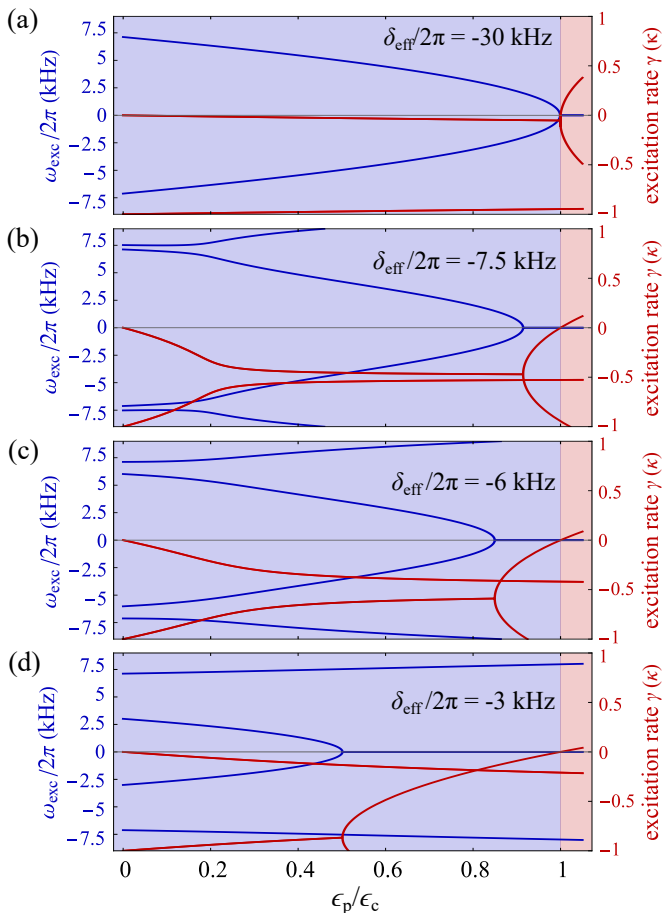


FIG. 2. Calculated excitation frequency (blue) and excitation rate (red) of the lower and upper polariton modes for an effective detuning of (a) $\delta_{\text{eff}}/2\pi = -30$ kHz, (b) $\delta_{\text{eff}}/2\pi = -7.5$ kHz, (c) $\delta_{\text{eff}}/2\pi = -6$ kHz, and (d) $\delta_{\text{eff}}/2\pi = -3$ kHz. (a): The lower polariton mode at zero pump strength shows an excitation frequency of $\pm\omega_{\text{rec}}/\pi = \pm 7.1$ kHz, which identifies its atomic character for $\epsilon_p = 0$. As ϵ_p increases, its frequency falls to zero very close to the critical pump strength. The upper polariton mode resides at values of the excitation frequency around $\pm\delta_{\text{eff}}/2\pi = \pm 30$ kHz for all values of the pump strength and hence appears outside of the plot range. The excitation rates are negative nearly all the way to the critical pump strength. (b): The upper and the lower polariton modes are shown. As in (a) and (b), at $\epsilon_p = 0$ the upper mode and the lower mode show purely photonic and atomic character, respectively. The lower polariton mode starts with an excitation frequency $\pm\omega_{\text{rec}}/\pi$ at $\epsilon_p = 0$ as in (a) but clearly falls to zero before the critical pump strength is reached. (c) and (d): For $\epsilon_p = 0$, the upper (lower) polariton mode acquires pure atomic (photonic) character. On a large part of the pump strength axis, zero excitation frequency is found for the lower polariton, while all excitation rates are negative below the critical pump strength.

excitation rate, as this determines whether small deviations from the equilibrium are self-reinforcing. In the case of a positive excitation rate, the system is pulled into the SR phase. While for a negative excitation rate, an excitation to the SR phase is damped, causing the system to remain in the NP.

The results of the two-mode stability analysis are shown in Figs.2(a-d). In the far detuned case $|\delta_{\text{eff}}| \gg \omega_{\text{rec}}$, approximately realized in Fig.2(a), the lower polariton mode contains a very small admixture of the photonic component, and its excitation energy undergoes a roton-like mode softening [35],

$$\omega_{\text{exc}} = 2\omega_{\text{rec}} \sqrt{1 - \frac{\epsilon_p}{\epsilon_c}}, \quad (1)$$

with the excitation energy reaching zero at a pump strength nearly coinciding with the critical pump strength ϵ_c . As seen in Figure 2(a) (red graph), the associated excitation rate γ is initially drawn to negative values before splitting into two branches very near to the critical pump strength, with the upper branch becoming positive exactly at the critical pump strength ϵ_c . This behavior resembles previous observations in the instantaneous LIRI regime [35, 37].

In the near-resonant regime $|\delta_{\text{eff}}| \lesssim 2\omega_{\text{rec}}$, Figure 2(b-d), the admixture of the photonic component to the polariton mode becomes significantly larger as the characteristic photon energy $\hbar|\delta_{\text{eff}}|$ approaches the relevant atomic energy $2\hbar\omega_{\text{rec}}$. While decay of the atomic momentum modes is negligible on experimental timescales, the photons decay from the cavity at a rate of $1/(2\pi\kappa)$. Analytical calculations using the Dicke model for the resonant case $|\delta_{\text{eff}}| = 2\omega_{\text{rec}}$ shown in the supplemental material [36] suggest an interpretation that the dissipation effectively shifts the excitation rate curve by $-\kappa/2$, which means that the critical pump strength is pushed to higher values than in the case for $\kappa = 0$. This is consistent with previous results for the polariton frequencies [38, 39]. This effect becomes more pronounced as $|\delta_{\text{eff}}|$ decreases and leads to a regime in which the lower polaritonic excitation frequency ω_{exc} reaches zero far below ϵ_c . However, due to the dissipation-induced overdamping, $\gamma < 0$, the system remains in the homogeneous NP despite the vanishing energy cost for the excitation of the lower polariton mode. We refer to this mode as a *polaritonic zero-energy excitation mode*.

We measure the excitation energy of the polariton modes using a form of Bragg spectroscopy [40, 41]. To probe this excitation energy, we utilise a probe beam directly on the cavity axis (the z -axis), in addition to the previously-introduced transverse pump along the y -axis. This probe beam is referred to in the following as the longitudinal pump with frequency ω_l , see Figure 1(a). When the frequency detuning δ_{lt} between the two pumps is equal to the energy required to excite one of the polariton modes, the atoms can scatter light from one pump into the other, depending on the relative detuning, and create excitations of the polariton mode, as illustrated in Figures 1(a) and 1(b). As the atomic component of the polariton modes is a superposition of the $|\pm 1, \pm 1\rangle$ momentum modes, this results in the build-up of a weak density grating, which fulfils the Bragg condition for constructive interference of scattering from the transverse pump into the cavity. In this case, this scattering process is temporary, as the modes are subject to damping, and the process is not self-reinforcing below ϵ_c . Thus, Bragg

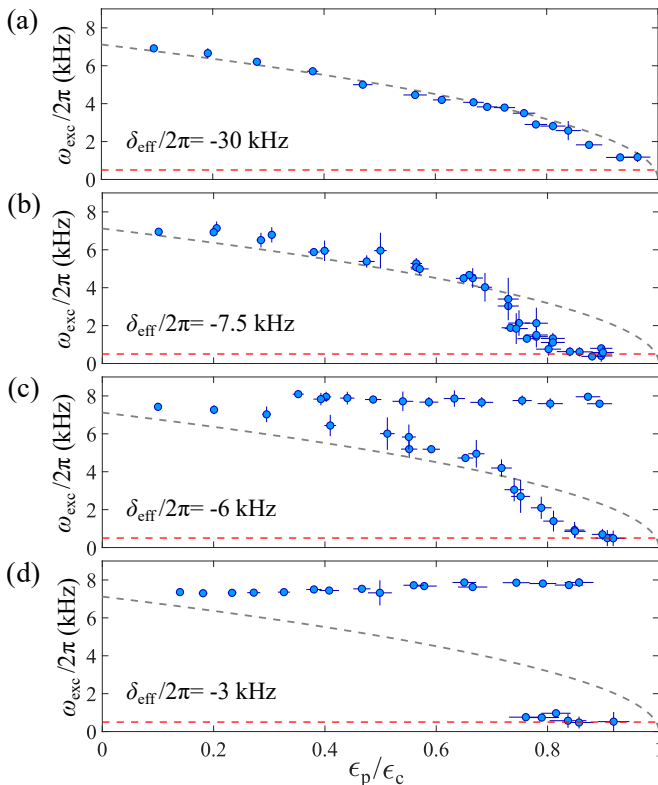


FIG. 3. Excitation spectra measured for an effective detuning of (a) $\delta_{\text{eff}}/2\pi = -30$ kHz, (b) $\delta_{\text{eff}}/2\pi = -7.5$ kHz, (c) $\delta_{\text{eff}}/2\pi = -6$ kHz, and (d) $\delta_{\text{eff}}/2\pi = -3$ kHz. The lowest frequency that can be accurately resolved with our experimental protocol, 500 Hz, is marked by a red dashed line, and the square-root behavior predicted for the far-detuned regime as per equation Eq.(1) is shown in grey. (a) shows the mode softening of the lower polariton mode as the transverse pump strength ϵ_p approaches the self-organisation threshold ϵ_c . (b) shows the formation of an overdamped excitation mode, as the excitation energy of the lower polariton mode falls off to zero and remains at zero before the transverse pump strength ϵ_p reaches the critical pump strength ϵ_c . In (c) and (d), for $\epsilon_p = 0$, the upper (lower) polariton mode acquires pure atomic (photonic) character. Away from $\epsilon_p = 0$, both modes possess sufficient atomic admixture to be observed.

spectroscopy can be used to determine the excitation energy of the momentum modes by determining the detuning δ_{lt} at which the most atoms are excited into the polariton mode, and correspondingly, the most transverse pump light is scattered into the cavity. The highest intensity of light scattered into the cavity occurs when the detuning matches the corresponding excitation energy, $\delta_{\text{lt}} = \hbar\omega_{\text{exc}}$. The results are presented in Figure 3. The detailed protocol for how we extract ω_{exc} from the measured intracavity photon number N_p can be found in supplementary material [36].

In the far-detuned regime $|\delta_{\text{eff}}| \gg \omega_{\text{rec}}$, at an effective detuning of $\delta_{\text{eff}}/2\pi = -30$ kHz, we obtain the excitation spectrum shown in Fig.3(a). The excitation energy of the lower polariton mode falls off in good agreement with Eq.1, which

is also captured by our two-mode stability analysis shown in Fig.2(a). This shows the expected behavior for a small admixture of the photonic component to the lower polariton mode, with the excitation rate falling off to zero close to ϵ_c . The small deviation close to ϵ_c as compared to the results for a significantly larger κ [35] is attributed to a larger admixture of the photonic component to the lowest polariton mode in our system, which could contribute additional damping. This is further supported by our excitation spectrum measurements for an effective detuning of $\delta_{\text{eff}}/2\pi = -15$ kHz (see supplementary material [36]), which are closer to the cavity resonance and differ more from the behavior predicted by Eq. 1 for the $|\delta_{\text{eff}}| \gg \omega_{\text{rec}}$ regime.

When the transverse pump is near-resonant, $|\delta_{\text{eff}}| \lesssim 2\omega_{\text{rec}}$, we see significant deviations from the instantaneous LIRI prediction of Eq. 1, as the softening of the polaritonic zero-energy excitation mode is observed below ϵ_c . This can be seen clearly in Figs.3(b-d) as the lower polariton excitation frequency falls close to zero frequency at $\epsilon_p/\epsilon_c \approx 0.8$. Due to the digital bandpass filter we applied to the measured photon number, we cannot experimentally resolve frequencies below 500 Hz, indicated by red dashed lines in Figs.3(a-d). The results of the excitation frequency tending towards zero are also confirmed theoretically by the two-mode stability analysis, the dynamical multi-mode simulations (see supplementary material [36]), and the observed trajectory of the data. This observation verifies the presence of a polaritonic zero-energy excitation mode, which is accessible due to the recoil resolving ultralow bandwidth of our optical cavity.

Since the fundamental cavity mode excitation in the absence of a pump is $\hbar\delta_{\text{eff}}$, it is interesting to explore the case when the cavity photon excitation energy is slightly below the atomic excitation energy, which is the case for $\delta_{\text{eff}}/2\pi = -6$ kHz. This results in a strong mixture of atomic and photonic components for both upper and lower polaritonic modes as the transverse pump strength increases. In Fig.3(c), we observe two polaritonic modes with different excitation energies that deviate significantly from each other beyond $\epsilon_p/\epsilon_c = 0.3$ with one increasing further and the other tending towards zero at $\epsilon_p/\epsilon_c \approx 0.80$. This result heralds our observation of both upper and lower polaritonic modes. While the upper polaritonic mode was also predicted for $\delta_{\text{eff}}/2\pi = -7.5$ kHz in Fig.2(b), we were unable to verify it experimentally because our measurement protocol is primarily sensitive to polaritonic modes with a significant atomic character. Therefore, the detection of both the upper and lower polariton modes throughout the excitation spectrum confirms this strong admixture. This is further corroborated by the absence of a multi-peak structure in the excitation curves from the dynamical multi-mode simulations, which are presented in the supplementary material [36].

For smaller detunings, $|\delta_{\text{eff}}| < 2\omega_{\text{rec}}$, for example, at $\delta_{\text{eff}}/2\pi = -3$ kHz, the deviations from the instantaneous LIRI regime become more pronounced, as is shown in Fig.3(d). Here, we observe an upper polariton mode with an excitation frequency that begins at $\omega_{\text{exc}} \approx 2\omega_{\text{rec}}$ at $\epsilon_p = 0$,

and increases from there to around 8 kHz. At a transverse pump strength of $\epsilon_p/\epsilon_c \geq 0.75$, a second mode appears with an excitation frequency that remains around zero and elicits a significantly stronger response than the upper polariton mode, which significantly weakens past this point for the entire range of parameters where the lower polariton mode can be detected. Below this pump strength, this mode, which is predicted in the two-mode stability analysis in Figure 2(d), is not observable with the applied experimental protocol. While this may provide some indication as to the evolution of the atomic and photonic components of the polaritonic modes with ϵ_p/ϵ_c in the near-resonant regime, more extensive simulations, including a full eigenfunction analysis, would be required to confirm this, which goes beyond the scope of this work.

In conclusion, in the normal phase of the open Dicke model, implemented in an atom cavity platform, we experimentally observed a polaritonic zero-energy excitation mode, for which, despite vanishing excitation energy, no instability of the normal phase arises. Theoretical analysis confirms that the weak dissipation in the photonic sector, with the intracavity field decay rate being smaller than the photon recoil frequency, is responsible for the observations. Our work shows an interesting interplay between dissipation and infinite range many-body interaction and their implications for phase transitions in driven-dissipative quantum systems.

We thank J. Klinner, M. Wolke, J. Skulte, and L. Mathey for their support during the early stages of the project. We thank T. Donner, J. Marino, S. B. Jäger, and C. Zimmermann for fruitful discussions during the course of this project. This work was funded by the QuantERA II Program that has received funding from the European Union's Horizon 2020 research and innovation program under Grant Agreement No. 101017733, the Deutsche Forschungsgemeinschaft (DFG, German Research Foundation) "SFB-925" project 170620586, and the Cluster of Excellence "Advanced Imaging of Matter" (EXC 2056), Project No. 390715994. The project is co-financed by ERDF of the European Union and by "Fonds of the Hamburg Ministry of Science, Research, Equalities, and Districts (BWFGB)". J.G.C. acknowledges support from the DOST-ASTI's COARE high-performance computing facility.

* These authors have contributed equally to this work.

† hans.g.kessler@gmail.com

‡ andreas.hemmerich@uni-hamburg.de

- [1] H. Ritsch, P. Domokos, F. Brennecke, and T. Esslinger, Cold atoms in cavity-generated dynamical optical potentials, *Rev. Mod. Phys.* **85**, 553 (2013).
- [2] F. Mivehvar, F. Piazza, T. Donner, and H. Ritsch, Cavity qed with quantum gases: new paradigms in many-body physics, *Advances in Physics* **70**, 1–153 (2021).
- [3] P. Horak, G. Hechenblaike, K. M. Gheri, H. Stecher, and H. Ritsch, Cavity-induced atom cooling in the strong coupling regime, *Phys. Rev. Lett.* **79**, 4974 (1997).
- [4] V. Vuletić and S. Chu, Laser cooling of atoms, ions, or molecules by coherent scattering, *Phys. Rev. Lett.* **84**, 3787 (2000).
- [5] P. Maunz, T. Puppe, I. Schuster, N. Syassen, P. W. H. Pinkse, and G. Rempe, Cavity cooling of a single atom, *Nature* **428**, 50–52 (2004).
- [6] T. P. Purdy, D. W. C. Brooks, T. Botter, N. Brahms, Z. Ma, and D. M. Stamper-Kurn, Tunable cavity optomechanics with ultracold atoms, *Phys. Rev. Lett.* **105**, 133602 (2010).
- [7] M. Aspelmeyer, T. J. Kippenberg, and F. Marquardt, Cavity optomechanics, *Rev. Mod. Phys.* **86**, 1391 (2014).
- [8] F. Brennecke, S. Ritter, T. Donner, and T. Esslinger, Cavity optomechanics with a bose-einstein condensate, *Science* **322**, 235–238 (2008).
- [9] H. Gothe, T. Valenzuela, M. Cristiani, and J. Eschner, Optical bistability and nonlinear dynamics by saturation of cold yb atoms in a cavity, *Phys. Rev. A* **99**, 013849 (2019).
- [10] H. Keßler, J. Klinder, M. Wolke, and A. Hemmerich, Optomechanical atom-cavity interaction in the sub-recoil regime, *New Journal of Physics* **16**, 53008 (2014).
- [11] E. J. Davis, A. Periwal, E. S. Cooper, G. Bentsen, S. J. Evered, K. Van Kirk, and M. H. Schleier-Smith, Protecting spin coherence in a tunable heisenberg model, *Phys. Rev. Lett.* **125**, 060402 (2020).
- [12] V. D. Vaidya, Y. Guo, R. M. Kroeze, K. E. Ballantine, A. J. Kollár, J. Keeling, and B. L. Lev, Tunable-range, photon-mediated atomic interactions in multimode cavity qed, *Phys. Rev. X* **8**, 011002 (2018).
- [13] H. Keßler, P. Kongkhambut, C. Georges, L. Mathey, J. G. Cosme, and A. Hemmerich, Observation of a dissipative time crystal, *Phys. Rev. Lett.* **127**, 043602 (2021).
- [14] P. Kongkhambut, J. Skulte, L. Mathey, J. G. Cosme, A. Hemmerich, and H. Keßler, Observation of a continuous time crystal, *Science* **377**, 670 (2022).
- [15] J. Klinder, H. Keßler, M. R. Bakhtiari, M. Thorwart, and A. Hemmerich, Observation of a superradiant mott insulator in the dicke-hubbard model, *Physical Review Letters* **115**, 10.1103/physrevlett.115.230403 (2015).
- [16] R. Landig, L. Hruby, N. Dogra, M. Landini, R. Mottl, T. Donner, and T. Esslinger, Quantum phases from competing short- and long-range interactions in an optical lattice, *Nature* **532**, 476–479 (2016).
- [17] R. H. Dicke, Coherence in spontaneous radiation processes, *Phys. Rev.* **93**, 99 (1954).
- [18] A. T. Black, H. W. Chan, and V. Vuletić, Observation of collective friction forces due to spatial self-organization of atoms: From rayleigh to bragg scattering, *Phys. Rev. Lett.* **91**, 203001 (2003).
- [19] F. Piazza and P. Strack, Umklapp superradiance with a collisionless quantum degenerate fermi gas, *Physical Review Letters* **112**, 10.1103/physrevlett.112.143003 (2014).
- [20] J. Keeling, M. J. Bhaseen, and B. D. Simons, Fermionic superradiance in a transversely pumped optical cavity, *Phys. Rev. Lett.* **112**, 143002 (2014).
- [21] P. Wang, L. Deng, E. W. Hagley, Z. Fu, S. Chai, and J. Zhang, Observation of collective atomic recoil motion in a degenerate fermion gas, *Phys. Rev. Lett.* **106**, 210401 (2011).
- [22] V. Helsen, T. Zewtler, F. Mivehvar, E. Colella, K. Roux, H. Konishi, H. Ritsch, and J.-P. Brantut, Density-wave ordering in a unitary fermi gas with photon-mediated interactions, *Nature* **618**, 716–720 (2023).
- [23] K. Baumann, C. Guerlin, F. Brennecke, and T. Esslinger, Dicke quantum phase transition with a superfluid gas in an optical cavity, *Nature* **464**, 1301–1306 (2010).
- [24] D. Nagy, G. Kónya, G. Szirmai, and P. Domokos, Dicke-model

- phase transition in the quantum motion of a bose-einstein condensate in an optical cavity, *Phys. Rev. Lett.* **104**, 130401 (2010).
- [25] J. Klinder, H. Keßler, M. Wolke, L. Mathey, and A. Hemmerich, Dynamical phase transition in the open dicke model, *Proceedings of the National Academy of Sciences* **112**, 3290 (2015).
- [26] Z. Gong, R. Hamazaki, and M. Ueda, Discrete time-crystalline order in cavity and circuit qed systems, *Physical Review Letters* **120**, 10.1103/physrevlett.120.040404 (2018).
- [27] R. Chitra and O. Zilberberg, Dynamical many-body phases of the parametrically driven, dissipative dicke model, *Phys. Rev. A* **92**, 023815 (2015).
- [28] P. Kongkhambut, J. G. Cosme, J. Skulte, M. A. Moreno Armijos, L. Mathey, A. Hemmerich, and H. Keßler, Observation of a phase transition from a continuous to a discrete time crystal, *Reports on Progress in Physics* **87**, 080502 (2024).
- [29] J. Skulte, P. Kongkhambut, H. Keßler, A. Hemmerich, L. Mathey, and J. G. Cosme, Realizing limit cycles in dissipative bosonic systems, *Phys. Rev. A* **109**, 063317 (2024).
- [30] H. Keßler, J. G. Cosme, M. Hemmerling, L. Mathey, and A. Hemmerich, Emergent limit cycles and time crystal dynamics in an atom-cavity system, *Phys. Rev. A* **99**, 053605 (2019).
- [31] F. Piazza and H. Ritsch, Self-ordered limit cycles, chaos, and phase slippage with a superfluid inside an optical resonator, *Phys. Rev. Lett.* **115**, 163601 (2015).
- [32] K. Hepp and E. H. Lieb, On the superradiant phase transition for molecules in a quantized radiation field: the dicke maser model, *Annals of Physics* **76**, 360 (1973).
- [33] J. Klinder, H. Keßler, C. Georges, J. Vargas, and A. Hemmerich, Bose-Einstein condensates in an optical cavity with sub-recoil bandwidth, *Applied Physics B: Lasers and Optics* **122**, 299 (2016).
- [34] K. Baumann, R. Mottl, F. Brennecke, and T. Esslinger, Exploring symmetry breaking at the dicke quantum phase transition, *Phys. Rev. Lett.* **107**, 140402 (2011).
- [35] R. Mottl, F. Brennecke, K. Baumann, R. Landig, T. Donner, and T. Esslinger, Roton-type mode softening in a quantum gas with cavity-mediated long-range interactions, *Science* **336**, 1570 (2012).
- [36] See Supplemental Material for further information about the experiment, the two-mode stability analysis of the system below the critical threshold, the dynamic multi-mode simulations and more detail on the applied measurement protocol.
- [37] R. Landig, F. Brennecke, R. Mottl, T. Donner, and T. Esslinger, Measuring the dynamic structure factor of a quantum gas undergoing a structural phase transition, *Nature Communications* **6**, 10.1038/ncomms8046 (2015).
- [38] F. Dimer, B. Estienne, A. S. Parkins, and H. J. Carmichael, Proposed realization of the Dicke-model quantum phase transition in an optical cavity QED system, *Phys. Rev. A* **75**, 013804 (2007).
- [39] R. D. Jara, D. F. Salinel, and J. G. Cosme, Theory of parametric resonance for discrete time crystals in fully connected spin-cavity systems, *Phys. Rev. A* **109**, 042212 (2024).
- [40] J. Stenger, S. Inouye, A. P. Chikkatur, D. M. Stamper-Kurn, D. E. Pritchard, and W. Ketterle, Bragg spectroscopy of a bose-einstein condensate, *Physical Review Letters* **82**, 4569–4573 (1999).
- [41] P. T. Ernst, S. Götze, J. S. Krauser, K. Pyka, D.-S. Lühmann, D. Pfannkuche, and K. Sengstock, Probing superfluids in optical lattices by momentum-resolved bragg spectroscopy, *Nature Physics* **6**, 56–61 (2009).

**Supplemental Materials for
Observation of a zero-energy excitation mode in the open Dicke model**

Anton Bölian,^{1,*} Phatthamon Kongkhambut,^{1,2,3,*} Christoph Georges,¹ Roy D. Jara Jr.,⁴ José Vargas,¹ Jens Klinder,¹ Jayson G. Cosme,⁴ Hans Keßler,^{1,†} and Andreas Hemmerich^{1,5,‡}

¹*Center for Optical Quantum Technologies and Institute for Quantum Physics, Universität Hamburg, 22761 Hamburg, Germany*

²*Quantum Simulation Research Laboratory, Department of Physics and Materials Science,
Faculty of Science, Chiang Mai University, Chiang Mai, 50200, Thailand*

³*Thailand Center of Excellence in Physics, Office of the Permanent Secretary,
Ministry of Higher Education, Science, Research and Innovation, Thailand*

⁴*National Institute of Physics, University of the Philippines, Diliman, Quezon City 1101, Philippines*

⁵*The Hamburg Center for Ultrafast Imaging, Luruper Chaussee 149, 22761 Hamburg, Germany*

(Dated: February 18, 2025)

arXiv:2502.12155v1 [cond-mat.quant-gas] 17 Feb 2025

* These authors have contributed equally to this work.

† hans.g.kessler@gmail.com

‡ andreas.hemmerich@uni-hamburg.de

I. EXPERIMENTAL DETAILS

The experimental setup consists of a Bose-Einstein condensate of $N_a = 40 \cdot 10^3$ ^{87}Rb atoms, magnetically confined in a magnetic trap with harmonic trap frequencies of $(\omega_x, \omega_y, \omega_z) = 2\pi \cdot (83.0, 72.2, 23.7)$ Hz. These atoms are prepared in the $|5^2S_{1/2}, F = 2, m_f = 2\rangle$ hyperfine substate and coupled to a single mode of a high-finesse recoil-resolved optical cavity with a field decay rate of $\kappa = 2\pi \cdot 3.60$ kHz, which is on the same scale as the recoil frequency $\omega_{\text{rec}} = 2\pi \cdot 3.55$ kHz at the chosen pump wavelength λ_p . The transverse pump, which is used to control the coupling strength between the atoms and the cavity mode, is set to a wavelength of $\lambda_p = 803.26$ nm, far-red detuned with respect to the relevant atomic transitions at 794.98 and 780.24 nm, thus we operate in the dispersive regime. For a light shift per photon of $U_0 = -2\pi \cdot 0.34$ Hz per photon, the total dispersive shift for the coupling with the σ^- polarisation is equal to $\delta_- = \frac{N_a U_0}{2}$. Thus, we obtain the effective detuning $\delta_{\text{eff}} = \delta_c - \delta_-$, containing the dispersive shift.

II. CAVITY FIELD DETECTION

In our experiment, we use two methods to detect the light leaking out of the cavity. On one side, we detect the light transmitted by the high-reflecting mirror with a single-photon counting module (SPCM), which allows us to measure the intensity of the transmitted intracavity field and longitudinal pump signal. On the other side of the cavity, we detect the cavity leakage light using a balanced heterodyne setup, which employs a split-off branch of the transverse pump beam as a local reference. The beating signal generated by these two beams allows us to determine the time-resolved intracavity photon number $N_p(t)$ and the phase difference between the pump beam and the intracavity light field.

III. ATOM-CAVITY MODEL

In the following, we will analyze the atom-cavity Hamiltonian, going through it term-by-term and discussing these individually. We restrict our analysis to two dimensions, as the transverse pump and intracavity light field run along these directions, and almost all the dynamics in the system take place within this plane. In this approximation, the full Hamiltonian is as follows:

$$\hat{H}_{\text{full}} = \hat{H}_c + \hat{H}_a + \hat{H}_{\text{aa}} + \hat{H}_{\text{int}} \quad (1)$$

The cavity term is described by the following equation,

$$\hat{H}_c = -\hbar\delta_c \hat{a}^\dagger \hat{a}, \quad (2)$$

wherein δ_c is the bare detuning between the transverse pump and the cavity resonance, and \hat{a} is the annihilation operator that annihilates a single photon in the cavity mode. The purely atomic term is given by

$$\hat{H}_a = \int \hat{\Psi}^\dagger(y, z) \left(-\frac{\hbar^2 \nabla^2}{2m} + \epsilon_p \cos^2(ky) \right) \hat{\Psi}(y, z) dydz, \quad (3)$$

where m is the mass of a rubidium 87 atom, ϵ_p is the transverse pump strength, and k is the wave vector associated with the transverse pump wavelength λ_p . The on-site interaction between the atoms is captured by

$$\hat{H}_{\text{aa}} = U_a \int \hat{\Psi}^\dagger(y, z) \hat{\Psi}^\dagger(y, z) \hat{\Psi}(y, z) \hat{\Psi}(y, z) dydz. \quad (4)$$

In this equation, $U_a = \sqrt{2\pi} a_s \hbar / m l_x$ is the effective two-dimensional scattering length along the $y - z$ directions and l_x is the harmonic oscillator length of the magnetic trap along the x direction. The interaction between the atoms and the cavity is described by the following term:

$$\hat{H}_{\text{int}} = \int \hat{\Psi}^\dagger(y, z) \left(\hbar U_0 \cos^2(kz) \hat{a}^\dagger \hat{a} + \hbar \sqrt{\hbar \epsilon_p U_0} \cos(ky) \cos(kz) (\hat{a}^\dagger + \hat{a}) \right) \hat{\Psi}(y, z) dydz, \quad (5)$$

where U_0 is the dispersive shift per intracavity photon. To simulate our system below the critical threshold, we perform a mean-field approximation, replacing the operators with their expectation values, and obtaining new equations of motion, which are as

follows, starting with the matter component:

$$i\hbar \frac{\partial}{\partial t} \Psi(y, z, t) = \left(-\frac{\hbar^2 \nabla^2}{2m} + \hbar U_0 |\alpha(t)|^2 \cos^2(kz) + \hbar U_0 |\alpha_p(t)|^2 \cos^2(ky) + 2\hbar U_0 \text{Re}(\alpha(t)) \alpha_p(t) \cos(kz) \cos(ky) \right) \Psi(y, z, t). \quad (6)$$

Meanwhile, the intracavity field is described by the following terms,

$$i\hbar \frac{\partial}{\partial t} = \hbar (-\delta_c + N_a U_0 \langle \cos^2(kz) \rangle - i\kappa) \alpha(t) + \hbar N_a U_0 \alpha_p \langle \cos(ky) \cos(kz) \rangle, \quad (7)$$

wherein the expectation values $\langle \dots \rangle$ are integrated over the volume of the BEC, weighted by its density. Following this approximation, we neglect the potential from the magnetic trap and perform a plane-wave expansion of the atomic wave function in the relevant $y - z$ plane:

$$\Psi(y, z, t) = \sum_{n,m} \phi_{n,m} e^{inky} e^{imkz}. \quad (8)$$

In this equation, $\phi_{n,m}$ are the normalised ($\sum_{n,m} |\phi_{n,m}|^2 = 1$) single-particle amplitudes of the momentum state $(p_y, p_z) = (m, n)\hbar k$. This leads to the following equation of motion for the atomic density:

$$i \frac{\partial}{\partial t} \phi_{n,m} = \left(\omega_{\text{rec}}(n^2 + m^2) + \frac{U_0 |\alpha|^2}{2} + \frac{U_0 |\alpha_p|^2}{2} \right) \phi_{n,m} + \frac{U_0}{4} |\alpha(t)|^2 (\phi_{n,m+2} + \phi_{n,m-2}) + \frac{U_0}{4} |\alpha_p(t)|^2 (\phi_{n+2,m} + \phi_{n-2,m}) + \frac{U_0}{4} \alpha_p(t) \text{Re}(\alpha(t)) (\phi_{n+1,m+1} + \phi_{n+1,m-1} + \phi_{n-1,m+1} + \phi_{n-1,m-1}), \quad (9)$$

and the following equation of motion for the cavity mode:

$$i\hbar \frac{\partial}{\partial t} \alpha = \left(-\delta_c + \frac{N_a U_0}{2} \left(\sum_{n,m} \text{Re}(\phi_{n,m} \phi_{n,m+2}^*) - 1 \right) - i\kappa \right) \alpha - i \frac{U_0 N_a}{4} \alpha_p(t) \left(\sum_{n,m} \phi_{n,m} (\phi_{n+1,m+1}^* + \phi_{n-1,m+1}^*) + \phi_{n,m}^* (\phi_{n+1,m+1} + \phi_{n-1,m+1}) \right). \quad (10)$$

When the system is in the normal phase, below the self-organisation threshold, we can restrict our analysis to the $|0, 0\rangle$ and a superposition of the $|\pm 1, \pm 1\rangle$ momentum modes, with $\phi_{1,1} = \frac{1}{2} (\phi_{1,1} + \phi_{1,-1} + \phi_{-1,1} + \phi_{-1,-1})$, which is justified below the critical threshold, as higher momentum modes do not play a significant role below ϵ_c . In the following, we rescale the intracavity amplitude to $|\beta|^2 = |\alpha|^2 U_0 / 4\omega_{\text{rec}}$ and the pump strength is rescaled to $\epsilon_p = |\alpha_p|^2 U_0 / \omega_{\text{rec}}$. Furthermore, we can reasonably approximate our state below the critical threshold as $\phi_{n,m} = \delta_{n,0} \delta_{m,0}$ and $\beta = 0$, i.e., 100% condensate occupation and no photons in the cavity mode. We then linearise the equations of motion 9 and 10 around this equilibrium state, and set the energy of $|0, 0\rangle$ to the zero point energy, allowing us to write these four linear equations as follows [1]:

$$i \frac{\partial}{\partial t} \begin{pmatrix} \beta \\ \beta^* \\ \phi_1 \\ \phi_1^* \end{pmatrix} = \begin{pmatrix} \delta_{\text{eff}} - i\kappa & 0 & -i \frac{N_a U_0}{4} \sqrt{\epsilon_p} & -i \frac{N_a U_0}{4} \sqrt{\epsilon_p} \\ 0 & -\delta_{\text{eff}} - i\kappa & -i \frac{N_a U_0}{4} \sqrt{\epsilon_p} & -i \frac{N_a U_0}{4} \sqrt{\epsilon_p} \\ i\omega_{\text{rec}} \sqrt{\epsilon_p} & -i\omega_{\text{rec}} \sqrt{\epsilon_p} & 2\omega_{\text{rec}} & 0 \\ -i\omega_{\text{rec}} \sqrt{\epsilon_p} & i\omega_{\text{rec}} \sqrt{\epsilon_p} & 0 & -2\omega_{\text{rec}} \end{pmatrix} \begin{pmatrix} \beta \\ \beta^* \\ \phi_1 \\ \phi_1^* \end{pmatrix} \quad (11)$$

By diagonalising this stability matrix and calculating its eigenvalues, one can separate out the real and imaginary parts of the eigenvalues, which correspond to the excitation energy $E_{\text{exc}} = \hbar\omega_{\text{exc}}$ and excitation rate γ of the mode. For $\epsilon_p = 0$, the modes are fully decoupled, and the eigenstates of the matrix are excitations of ϕ_1 and β , i.e., the atomic momentum state and the cavity mode. For nonzero ϵ_p , the eigenstates of this matrix are mixed atom-light excitations, or polariton modes. The degree that these modes mix depends on the detuning between the transverse pump and the cavity and on its relation to the cavity decay rate κ . The real and complex parts of the eigenvalues of this matrix are used to calculate the excitation energy and excitation rate of the polariton modes in the two-mode stability analysis in the main text.

IV. DICKE MODEL AND THE ANALYTICAL EXPRESSION FOR THE EXCITATION SPECTRA

To provide analytical insights into the mode softening of lower polariton at pump intensities lower than the critical value, we map the atom-cavity system onto the paradigmatic Dicke model. Specific details on the mapping can be found in Refs. [2, 3]. In the following, we simply highlight the important equations and the pertinent details are discussed in Ref. [4]. The open Dicke model is described by the Lindblad master equation [5],

$$\partial_t \hat{\rho} = -i \left[\frac{\hat{H}_{\text{DM}}}{\hbar}, \rho \right] + \kappa (2\hat{a}\hat{\rho}\hat{a}^\dagger - \{\hat{a}^\dagger\hat{a}, \hat{\rho}\}), \quad (12)$$

where the Hamiltonian reads

$$\frac{\hat{H}_{\text{DM}}}{\hbar} = \omega \hat{a}^\dagger \hat{a} + \omega_0 \hat{J}_z + \frac{2\lambda}{\sqrt{N}} (\hat{a} + \hat{a}^\dagger) \hat{J}_x. \quad (13)$$

The collective spin operators describing the matter sector approximated as two-level systems are \hat{J}_μ , the light-matter coupling strength is λ , the two-level transition frequency is ω_0 , and the photon frequency is ω . In terms of the original atom-cavity parameters, we have $\lambda = \sqrt{N_a \omega_{\text{rec}} \varepsilon |U_0|}/2$, where ε is the unitless pump intensity, $\omega_0 = 2\omega_{\text{rec}}$, and $\omega = -\delta_{\text{eff}}$. The critical light-matter coupling strength for the NP-SR phase transition is

$$\lambda_c = \frac{1}{2} \sqrt{\frac{\omega_0}{\omega} (\kappa^2 + \omega^2)}. \quad (14)$$

In the thermodynamic limit, we can use the Holstein-Primakoff transformation to obtain a linearised oscillator-like model (LOM) with a Hamiltonian given by

$$\frac{\hat{H}_{\text{LOM}}}{\hbar} = \omega \hat{a}^\dagger \hat{a} + \omega_0 \hat{b}^\dagger \hat{b} + \lambda (\hat{a}^\dagger + \hat{a}) (\hat{b} + \hat{b}^\dagger), \quad (15)$$

where \hat{b} is the bosonic operator corresponding to the matter sector. This Hamiltonian is akin to that of a system with coupled linear oscillators. In particular, using a semi-classical treatment where we treat \hat{a} and \hat{b} as complex numbers, the equations of motion for \hat{a} and \hat{b} accounting for photon dissipation takes the form [4]

$$\frac{\partial^2}{\partial t^2} \mathbf{x} + \begin{pmatrix} 2\kappa & 0 \\ 0 & 0 \end{pmatrix} \frac{\partial}{\partial t} \mathbf{x} + \begin{pmatrix} \omega^2 + \kappa^2 & 2\lambda\sqrt{\omega\omega_0} \\ 2\lambda\sqrt{\omega\omega_0} & \omega_0^2 \end{pmatrix} \mathbf{x} = 0, \quad (16)$$

where $\mathbf{x} = [x \ y]^T$ and

$$x = \frac{1}{\sqrt{2\omega}} (a + a^*), \quad p_x = i\sqrt{\frac{\omega}{2}} (a - a^*), \quad y = \frac{1}{\sqrt{2\omega_0}} (b + b^*), \quad p_y = i\sqrt{\frac{\omega_0}{2}} (b - b^*), \quad (17)$$

with $a = \langle \hat{a} \rangle$ and $b = \langle \hat{b} \rangle$, $a, b \in \mathbb{C}$. In this mapping, obtaining the polariton modes of the atom-cavity system is equivalent to finding the normal modes of the LOM, in which each decoupled mode corresponds to a polariton mode [4].

We can derive the normal modes of the LOM by first substituting the Ansatz

$$\mathbf{x} = \frac{1}{2} \exp(\Omega t) \begin{pmatrix} 1 & 1 \\ 1 & -1 \end{pmatrix} \mathbf{x}_0 = \frac{1}{2} \exp\left(-\frac{\kappa t}{2}\right) \exp(\Gamma t) \begin{pmatrix} 1 & 1 \\ 1 & -1 \end{pmatrix} \mathbf{x}_0, \quad (18)$$

where \mathbf{x}_0 is a constant vector, back to Eq. (16). This leads to a nonlinear eigenvalue problem of the form,

$$\mathcal{M}(\Gamma) \mathbf{x}_0 = 0, \quad \mathcal{M}(\Gamma) \equiv \begin{pmatrix} \omega^2 - \frac{1}{4} (\Delta_+^2 + \Delta_-^2) + \Gamma\kappa & \omega^2 - \frac{1}{4} (\Delta_+^2 + \Delta_-^2) + \Gamma\kappa \\ \omega^2 - \frac{1}{4} (\Delta_+^2 + \Delta_-^2) + \Gamma\kappa & \omega^2 - \frac{1}{4} (\Delta_+^2 + \Delta_-^2) + \Gamma\kappa \end{pmatrix}, \quad (19)$$

where $\Delta_\pm = \omega \pm \omega_0$ and,

$$\omega_\pm^2 = \frac{1}{4} (\Delta_+^2 + \Delta_-^2) + \frac{\kappa^2}{4} \pm \lambda \sqrt{\Delta_+^2 - \Delta_-^2}. \quad (20)$$

From Eq. (18) and Eq. (19), it follows that the complex normal mode frequencies are

$$\Omega = -\frac{\kappa}{2} + \Gamma_0(\omega, \omega_0), \quad (21)$$

where $\Gamma_0(\omega, \omega_0)$ are the complex roots of the characteristic polynomial of $\mathcal{M}(\Gamma)$, defined as

$$F(\Gamma) \equiv \det(\mathcal{M}(\Gamma)), \quad (22a)$$

$$F(\Gamma) = \left[\Gamma^2 + \frac{1}{2}(\omega^2 + \omega_0^2) - \frac{\kappa^2}{4} \right]^2 - \Gamma\kappa(\omega^2 - \omega_0^2) - \lambda'^2\omega_0^2(\kappa^2 + \omega^2) + \frac{1}{2}(\omega^2 + \omega_0^2)\kappa^2 - \frac{1}{4}(\omega^2 - \omega_0^2)^2. \quad (22b)$$

An analytical expression can be obtained in the resonant regime $\omega = \omega_0$ and, focusing on the lower polariton, the corresponding complex lower polariton frequency is given by

$$\Omega_{\text{LP}} = -\frac{\kappa}{2} + \Omega_0, \quad (23)$$

where

$$\Omega_0 = \sqrt{\frac{\kappa^2}{4} - \omega^2 + \omega\sqrt{\lambda'^2(\kappa^2 + \omega^2) - \kappa^2}} \quad (24)$$

and $\lambda' = \lambda/\lambda_c$. This expression is consistent with that from an eigenvalue analysis of the Lindbladian in Ref. [5]. Note that the structure of the normal mode solution being $\mathbf{x} \propto \exp(\Omega_{\text{LP}}t)\mathbf{x}_0$ means that the **excitation frequency** is $\omega_{\text{exc}} = \text{Im}[\Omega_{\text{LP}}]$ and the **excitation rate** is $\gamma = \text{Re}[\Omega_{\text{LP}}]$, which is opposite to the two-mode stability analysis described above. We point out this difference is just a matter of convention and that these two approaches can be made consistent by simply multiplying Ω_{LP} with i .

In Fig. 1(a), we present a good agreement between the numerical diagonalisation of the two-mode stability matrix Eq. (11) and the analytical expression Eq. (23) for the excitation frequency and rate in the resonant regime. From Eqs. (23) and (24), we can infer that γ becomes zero at the critical point $\lambda' = 1$ as expected. More importantly, we can see that the excitation frequency is solely dependent on Ω_0 in the resonant regime since $\omega_{\text{exc}} = \text{Im}[\Omega_{\text{LP}}] = \text{Im}[\Omega_0]$. In the absence of dissipation the ‘‘bare’’ polariton frequency is $\Omega_{\text{LP}} = \Omega_0 = \omega\sqrt{\lambda' - 1}$ and we find that both the excitation energy and rate become zero at the critical point. We can then interpret Eq. (23) as the dissipation not only modifying the bare polariton frequency Ω_0 but also, more importantly for the existence of the polaritonic zero-energy excitation mode, effectively decreasing the excitation rate by shifting the excitation rate curve by half of the dissipation rate $\kappa/2$. This leads to the excitation rate γ no longer coinciding with the excitation frequency ω_{exc} at $\lambda = \lambda_{\text{cr}}$. As the zero-crossing of γ gets pushed to higher values of λ owing to the dissipation-induced negative shift, the excitation frequency ω_{exc} becomes zero for $\lambda < \lambda_c$. The apparent mode softening of the lower polariton below the critical point can thus be attributed to dissipation.

While we can obtain an analytic expression for the polariton frequencies in the resonant regime, finding the roots of $F(\Gamma)$ in the general case of $\omega \neq \omega_0$ becomes intractable due to the presence of the $\Gamma\kappa(\omega^2 - \omega_0^2)$ cross-term. To obtain a closed-form approximation for the Γ_0 corresponding to the lower polariton in the small detuning case, we use the first iteration of the Newton-Rhaphson method, where we assume that

$$\Gamma_{0,\text{LP}}(\omega \neq \omega_0) \approx \Omega_0 - \frac{F(\Omega_0)}{\partial_{\Gamma}F(\Gamma)|_{\Gamma=\Omega_0}}, \quad (25)$$

with

$$F(\Omega_0) = (\omega^2 - \omega_0^2) \left[\lambda'^2(\kappa^2 + \omega^2) - \frac{\kappa^2}{2} - \omega\sqrt{\lambda'^2(\kappa^2 + \omega^2) - \kappa^2} - \Omega_0\kappa \right], \quad (26)$$

and

$$\frac{\partial F(\Gamma)}{\partial \Gamma} \Big|_{\Gamma=\Omega_0} = 4\omega\Omega_0\sqrt{\lambda'^2(\kappa^2 + \omega^2) - \kappa^2} - (\omega^2 - \omega_0^2)(\kappa + 2\Omega_0). \quad (27)$$

This assumption is justified since as the detuning between ω and ω_0 goes to zero, $\Delta_- \rightarrow 0$, $\Gamma_0 \rightarrow \Omega_0$. Thus, Eq. (25) should provide a good approximation for Γ_0 so long as the detuning is sufficiently small. With this, the lower polariton frequency for small detuning finally reads,

$$\Omega_{\text{LP}} = -\frac{\kappa}{2} + \Omega_0 - (\omega^2 - \omega_0^2)\Omega' \quad (28)$$

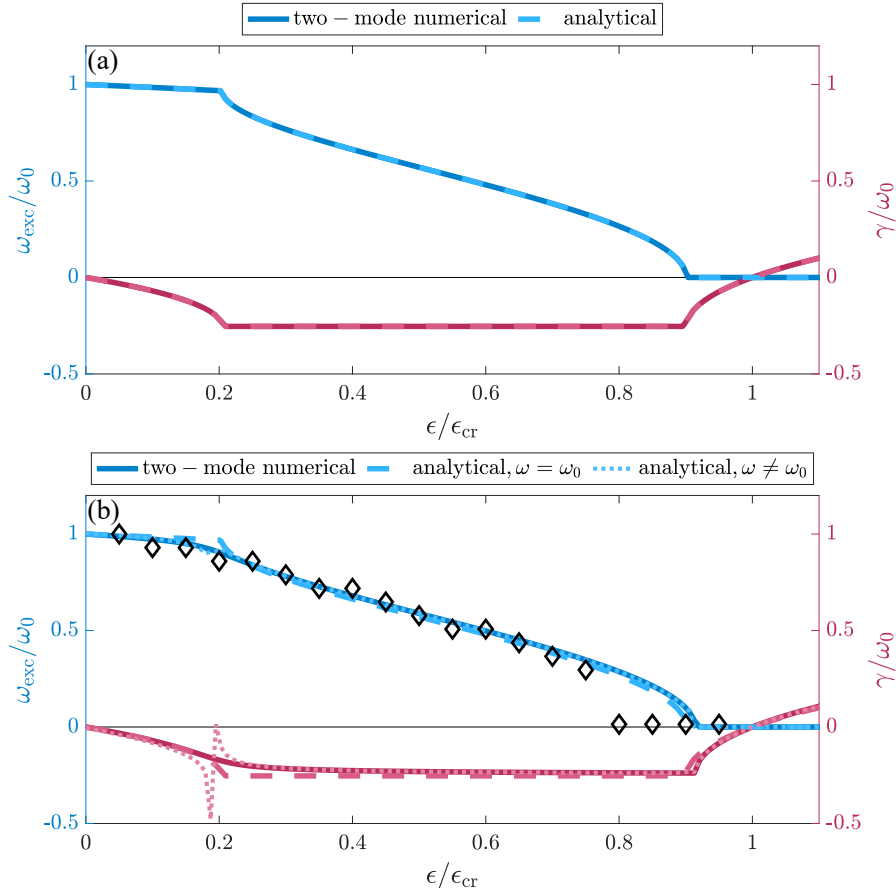


FIG. 1. Theoretical excitation rate and frequency for varying ϵ with (a) $|\delta_{\text{eff}}| = 2\omega_{\text{rec}}$ and (b) $\delta_{\text{eff}} = -2\pi \times 7.5$ kHz. The solid lines correspond to numerical diagonalisation of the stability matrix Eq. (11). The broken lines correspond to the analytical predictions Eqs. (23) and (28). The diamond markers in (b) denote the results from a full dynamical simulation of the multi-mode system discussed in the last section of the supplemental material.

where the correction due to the detuning between ω and ω_0 is

$$\Omega' = \frac{\lambda'^2(\kappa^2 + \omega^2) - \kappa^2/2 - \omega\sqrt{\lambda'^2(\kappa^2 + \omega^2) - \kappa^2} - \Omega_0\kappa}{4\omega\Omega_0\sqrt{\lambda'^2(\kappa^2 + \omega^2) - \kappa^2} - (\omega^2 - \omega_0^2)(\kappa + 2\Omega_0)}. \quad (29)$$

Note that by virtue of Eq. (21), the general structure of Ω_{LP} remains the same as in the resonant regime, wherein the dissipation introduces the $-\kappa/2$ shift in the excitation rate. This is further corroborated by the good agreement between $\omega = \omega_0$ and $\omega \neq \omega_0$ in the Fig. 1(b), which supports the interpretation that the existence of the polaritonic zero-energy excitation is due to dissipation. We also point out that the diamond markers in Fig. 1(b), which correspond to the numerical results from a full dynamical simulation of the longitudinal probing protocol using a multi-mode atom-cavity model (this will be discussed in the last section of the supplemental material), are in good agreement with the two-mode stability matrix simulation and the analytical results as given by Eq. (28), especially for small pump intensities. This further underpins the underlying dissipation-induced mechanism for the pre-critical point mode softening of the lower polariton. The deviations for larger ϵ suggest that the higher-momentum modes neglected in the two-mode and analytical descriptions become relevant in this regime. Nevertheless, the various theoretical approaches all agree that there is a polaritonic zero-energy excitation in the system.

V. DATA EVALUATION PROTOCOL

To experimentally determine the excitation energy at a fraction of the critical pump strength, $\epsilon_p < \epsilon_c$, we first determine the value of critical pump strength for a fixed detuning δ_{eff} . Thus, we fix the detuning δ_{eff} for an entire excitation spectrum, load the BEC into the cavity, and linearly ramp the transverse pump strength ϵ_p over the critical threshold with a constant gradient,

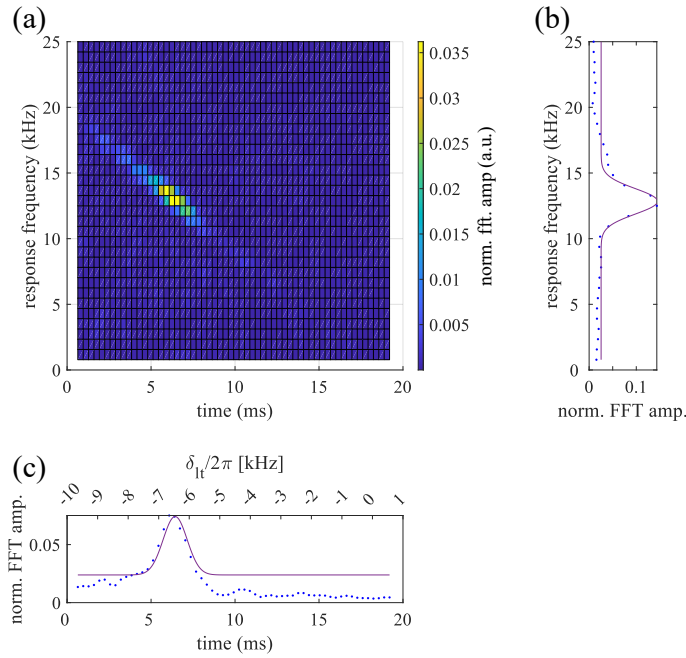


FIG. 2. (a) Single-sided spectrogram obtained from the time-resolved Fourier transform of the photon number N_p measured by the heterodyne detector for an effective detuning of $\delta_{\text{eff}}/2\pi = -15$ kHz, a transverse pump strength of $\epsilon_p/\epsilon_c = 0.2$ and a final longitudinal pump power of 8.0 pW in front of the cavity. (b) The sum of the normalised Fourier amplitudes within a given frequency range for all time bins is plotted against the response frequency. (c) The sum of the normalised Fourier amplitudes for all frequencies within one time bin plotted against the measurement time and detuning δ_{1t} . A Gaussian profile is fitted to (b) and (c) to separately determine the excitation energy from each method. The result from (c) is used to determine the excitation energy in the results shown here due to its higher precision, while the result from (b) is used as a reference value for post-selection.

without any involvement of the longitudinal pump. This measurement is repeated between measurements of the excitation energy to compensate for drifts in ϵ_c over time. Following this, to measure the excitation energy of the polariton mode, we load the BEC into the cavity and linearly increase the transverse pump to a fraction of the critical pump strength using a constant gradient and hold the pump strength at this value for 20 ms. After the ramp, we activate the longitudinal pump, linearly sweep the detuning between the longitudinal and the transverse pump from $\delta_{1t}/2\pi = -10$ to $+1$ kHz, and measure the photon number N_p in the cavity by detecting the light leaking out of the cavity using a balanced heterodyne detector. Subsequently, we apply a digital bandpass filter with a pass range between 500 Hz and 100 kHz to the detected photon number to remove both high-frequency noise and the offset added to the signal by the longitudinal pump light reflected by the cavity coupling mirror. After this, we apply a time-resolved Fourier transform to the filtered photon number, binning the data into 59 intervals and analysing the Fourier amplitude for the given frequency components during the sweep of δ_{1t} . At resonance, we would expect a beating frequency of $2\omega_{\text{exc}}$, as the longitudinal and transverse pumps beat at the position of the atoms, causing a density modulation at the position of the atoms of this frequency, which is then transferred to the light field. In addition to this, the signal, which has the frequency of the transverse pump, beats with the longitudinal pump on the heterodyne detector. These two modulations cause the photon number to oscillate at $2\omega_{\text{exc}}$ when the resonance condition is reached, and light is scattered from the density lattice into the cavity. We obtain the excitation energy ω_{exc} of the polariton mode from the detuning δ_{1t} that corresponds to the time during the scan at which the most transverse pump light is scattered by the density lattice into the cavity. This measurement is performed between 10 and 20 times for a fixed transverse pump strength, averaging over the results of the excitation energies from these measurements to determine ω_{exc} and repeated for different fractions of ϵ_p/ϵ_c to obtain an excitation spectrum.

VI. INTENSITY COMPENSATION SCHEME

In our experiment, we use an on-axis longitudinal pump to measure the excitation energy of the polariton modes. As we sweep the frequency of the longitudinal pump with respect to the transverse pump frequency, the coupling efficiency of the longitudinal pump with respect to the cavity changes. To maintain a longitudinal pump power in the cavity that is close to constant throughout an experimental sequence, we apply an intensity compensation scheme, which is shown in Figure 3: This protocol works as

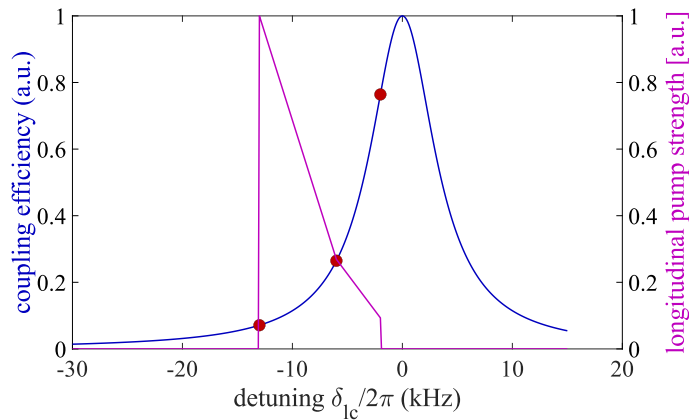


FIG. 3. Intensity compensation scheme applied to the longitudinal pump intensity to address the frequency-dependent coupling efficiency of the cavity for an effective detuning of $\delta_{\text{eff}}/2\pi = -3$ kHz. **Blue:** frequency-dependent coupling efficiency of the cavity for the TEM_{00} mode plotted against the detuning δ_{lc} between the longitudinal pump and the effective cavity resonance frequency, **red:** marked points in the scan range between which the longitudinal pump intensity is linearly decreased, and **pink:** longitudinal pump intensity after applying the compensation protocol.

follows: we calculate the inverse of the coupling efficiency of three points in the scan, here at $\delta_{lc}/2\pi = [-13, -6, -2]$ kHz for an effective transverse pump detuning of $\delta_{\text{eff}}/2\pi = -3$ kHz, which are $[0.0712, 0.2646, 0.7634]$ and the inverse $[14.04, 3.78, 1.31]$. These inverse values of the coupling efficiencies are normalised by dividing them by the smallest value, leading to the following compensation factors: $[10.72, 2.89, 1.00]$. We then return to the three detunings δ_{lt} marked in Figure 3, multiply the longitudinal pump strength set on the experimental control by the value corresponding to the frequency of those points, and apply a linear gradient of the longitudinal pump strength between neighbouring values, as shown in Figure 3. A linear ramp is chosen for its ease of implementation in the experimental control and its relative effectiveness, as can be seen in Figure 4. The intensity

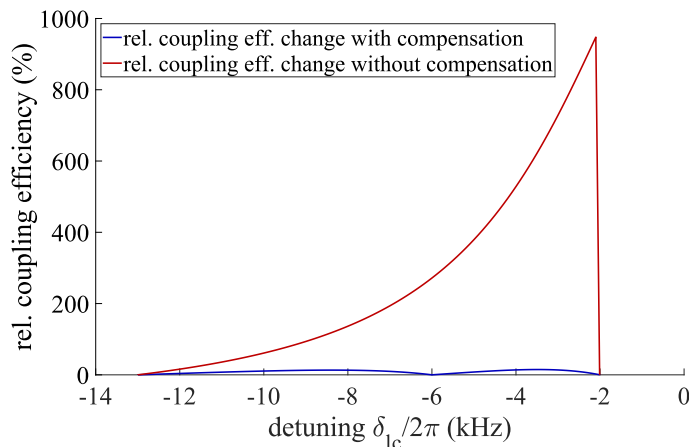


FIG. 4. Coupling efficiency with (blue) and without (red) application of the intensity compensation protocol, as presented in Figure 3, for an effective detuning of $\delta_{\text{eff}}/2\pi = -3$ kHz. The coupling efficiency change is relative to the value at $\delta_{lt}/2\pi = -13$ kHz.

compensation reduces the change in coupling efficiency δc_{eff} during a scan of δ_{lt} from $\delta c_{\text{eff}} = 947.6\%$ without application of the protocol to $\delta c_{\text{eff}} = 14.9\%$ with application of the protocol for an effective detuning of $\delta_{\text{eff}}/2\pi = -3$ kHz, which is well within the acceptable range for our measurements. For larger effective detunings, the deviations are even smaller, as the change in coupling efficiency that needs to be compensated decreases with increased detuning from the cavity resonance.

VII. ADDITIONAL EXCITATION SPECTRA

In addition to the results shown in the main manuscript, we recorded excitation spectra at effective detunings of $\delta_{\text{eff}}/2\pi = -15$ and -4 kHz, which are included alongside the spectra discussed in the main text in Figure 5(b) and (e) for completeness. For an effective detuning of $\delta_{\text{eff}}/2\pi = -15$ kHz, we observe that the deviation from the square-root behaviour predicted for a cavity

with significantly larger κ are more pronounced, the excitation spectrum at this detuning shows an intermediate stage between the excitation spectra at $\delta_{\text{eff}}/2\pi = -30$ and $\delta_{\text{eff}}/2\pi = -7.5$ kHz. The excitation spectrum at $\delta_{\text{eff}}/2\pi = -4$ kHz shows behaviour similar to the previously discussed results at $\delta_{\text{eff}}/2\pi = -3$ kHz, as both contain an upper polariton mode present throughout the entire spectrum and a lower mode with an excitation frequency close to 0 kHz.

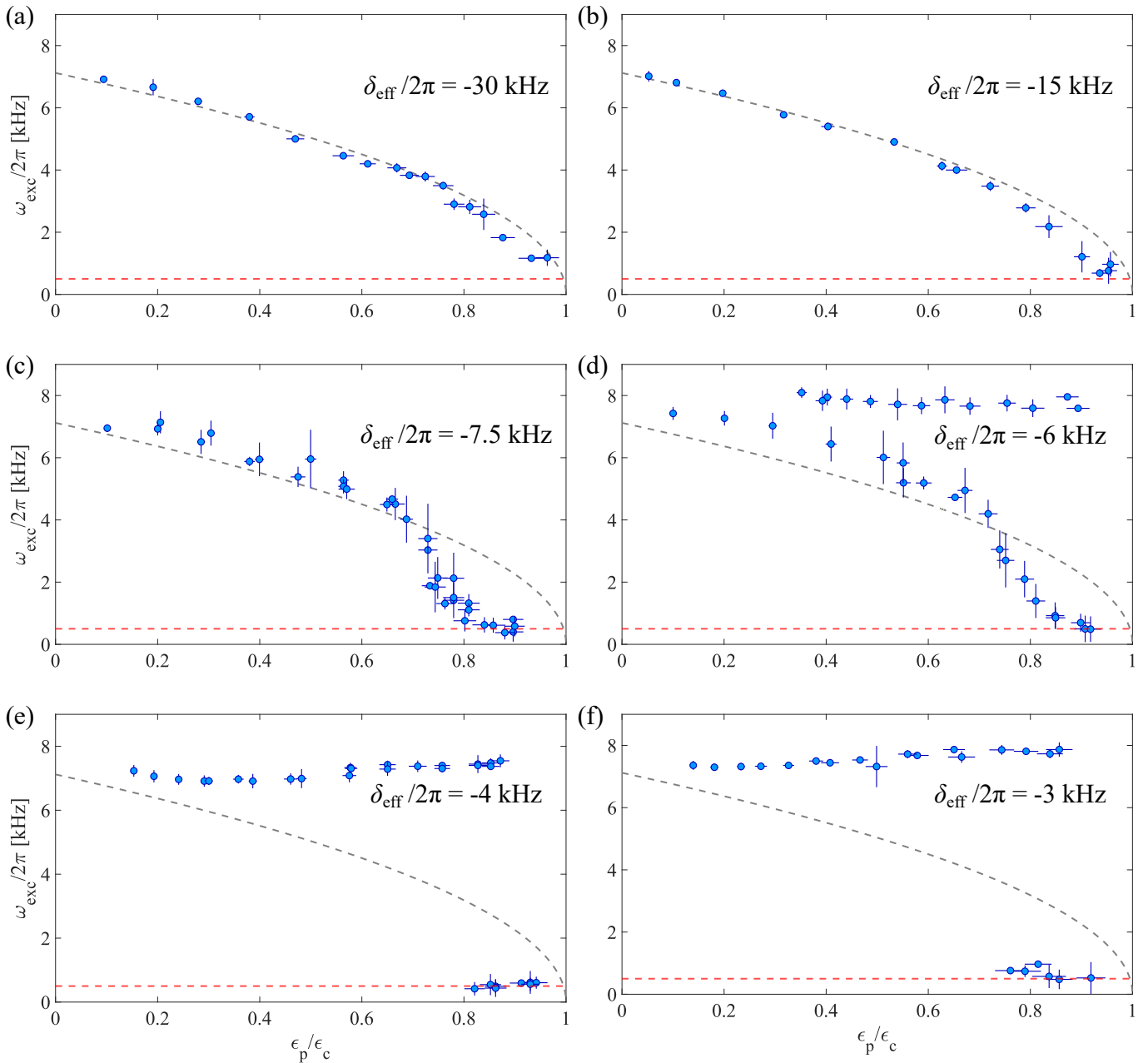


FIG. 5. Excitation spectra measured for effective detunings of (a) $\delta_{\text{eff}}/2\pi = -30$ kHz, (b) $\delta_{\text{eff}}/2\pi = -15$ kHz, (c) $\delta_{\text{eff}}/2\pi = -7.5$ kHz, (d) $\delta_{\text{eff}}/2\pi = -6$ kHz, (e) $\delta_{\text{eff}}/2\pi = -4$ kHz, and (f) $\delta_{\text{eff}}/2\pi = -3$ kHz as the transverse pump strength ϵ_p approaches the self-organisation threshold ϵ_c , showing the progression of the excitation spectrum from the far-detuned to the near-detuned regime. The lowest frequency that can accurately be resolved with our experimental protocol, 500 Hz, is marked by a red dashed line, and the square-root behaviour predicted for the far-detuned regime is shown in grey.

VIII. DYNAMIC MULTI-MODE SIMULATIONS

To simulate the exact conditions of our atom-cavity system applied for these measurements, we performed additional simulations, including both the longitudinal pump and higher momentum modes. These simulations were performed for all the

detunings shown in this manuscript, and are presented in Figure 6 and 7:

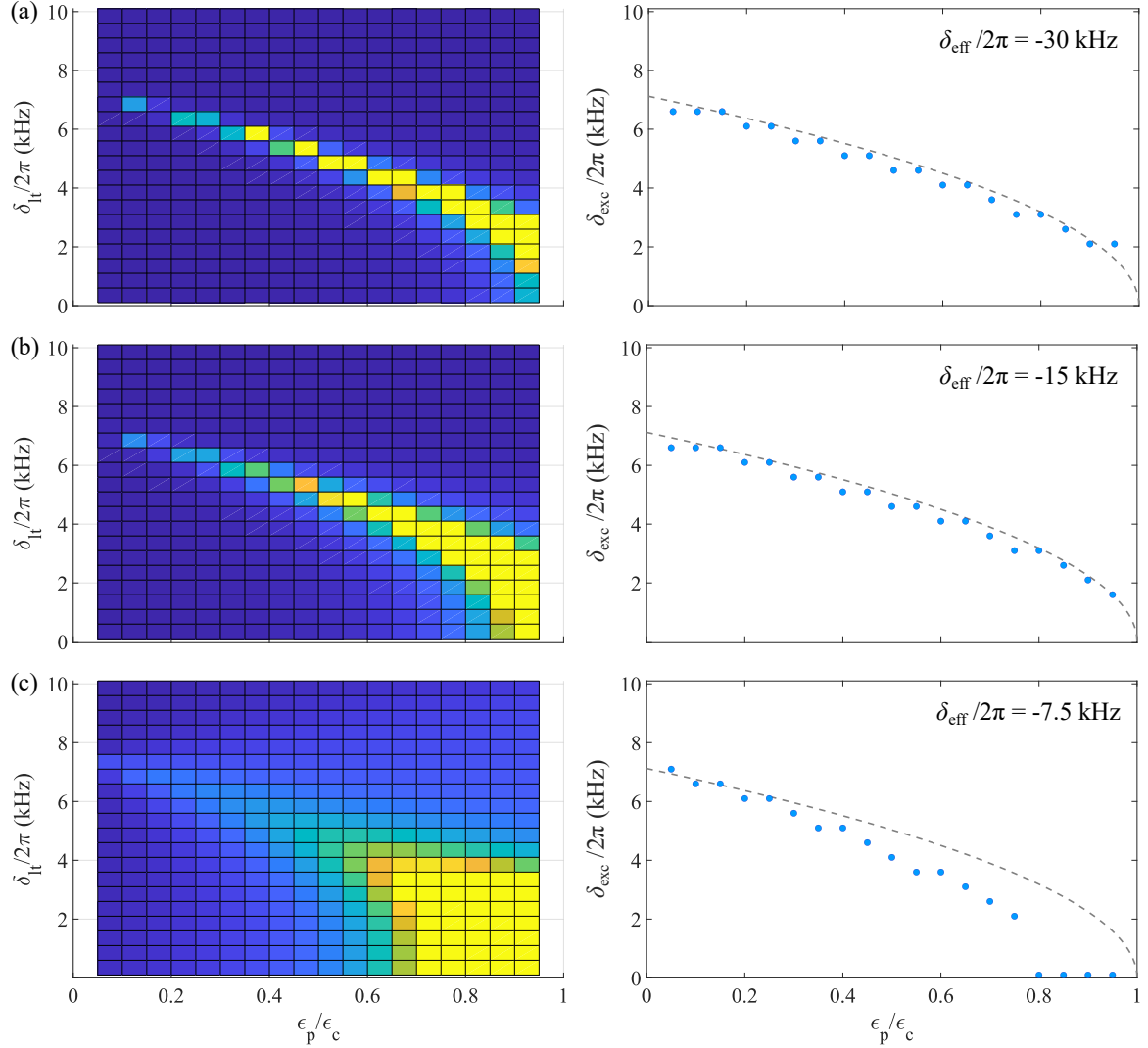


FIG. 6. Intracavity photon number resulting from the dynamic multimode simulations when varying the transverse pump strength ϵ_p/ϵ_c and the detuning between the longitudinal and the transverse pump δ_{lt} for effective detunings above $2\omega_{\text{rec}}$: (a) $\delta_{\text{eff}}/2\pi = -30$ kHz, (b) $\delta_{\text{eff}}/2\pi = -15$ kHz, and (c) $\delta_{\text{eff}}/2\pi = -7.5$ kHz. **Left:** total intracavity photon number for each δ_{lt} , and **right:** δ_{lt} at which the most longitudinal pump photons are scattered into the cavity for a fixed transverse pump strength ϵ_p/ϵ_c .

-
- [1] C. Georges, *The dynamical driven atom-cavity system: A realization beyond the open Dicke model*, Ph.D. thesis, University of Hamburg (2021).
 - [2] P. Kongkhambut, H. Keßler, J. Skulte, L. Mathey, J. G. Cosme, and A. Hemmerich, Realization of a Periodically Driven Open Three-Level Dicke Model, *Phys. Rev. Lett.* **127**, 253601 (2021).
 - [3] J. Skulte, P. Kongkhambut, H. Keßler, A. Hemmerich, L. Mathey, and J. G. Cosme, Realizing limit cycles in dissipative bosonic systems, *Phys. Rev. A* **109**, 063317 (2024).
 - [4] R. D. Jara, D. F. Salinel, and J. G. Cosme, Theory of parametric resonance for discrete time crystals in fully connected spin-cavity systems, *Phys. Rev. A* **109**, 042212 (2024).
 - [5] F. Dimer, B. Estienne, A. S. Parkins, and H. J. Carmichael, Proposed realization of the Dicke-model quantum phase transition in an optical cavity QED system, *Phys. Rev. A* **75**, 013804 (2007).

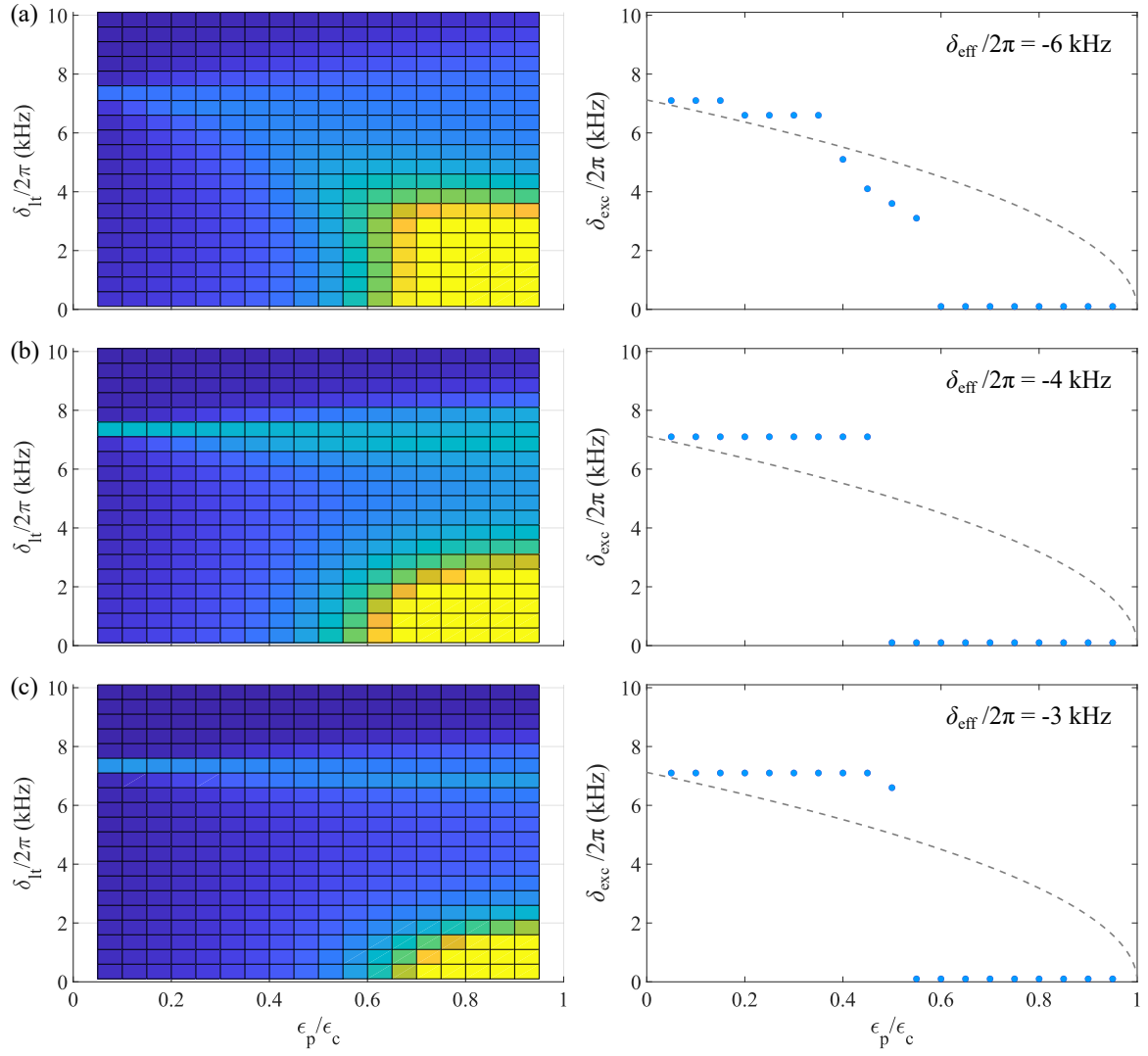


FIG. 7. Intracavity photon number resulting from the dynamic multimode simulations when varying the transverse pump strength ϵ_p/ϵ_c and the detuning between the longitudinal and the transverse pump δ_{lt} for effective detunings below $2\omega_{\text{rec}}$: (a) $\delta_{\text{eff}}/2\pi = -6$ kHz, (b) $\delta_{\text{eff}}/2\pi = -4$ kHz, and (c) $\delta_{\text{eff}}/2\pi = -3$ kHz. **Left:** total intracavity photon number for each δ_{lt} , and **right:** δ_{lt} at which the most longitudinal pump photons are scattered into the cavity for a fixed transverse pump strength ϵ_p/ϵ_c .